Version of Record: https://www.sciencedirect.com/science/article/pii/S0734743X21000270
Manuscript_3b916af2f52f25dafe6848083d2696e8

Microscopic Ejecta Measurements from Hypervelocity Impacts on Aluminum and Powdered Regolith Targets

Gil Shohet[a,*], Benjamin Estacio[a], Isaac Matthews[a], Sean A. Q. Young[a], Nicolas Lee[a], Sigrid Close[a]

[a]*Department of Aeronautics & Astronautics, Stanford University, Stanford, CA 94305, USA*

Abstract

Meteoroids and space debris pose a two-fold threat to spacecraft due to the risk of both mechanical damage from the impact and electrical damage from the impact-generated plasma, which produces electromagnetic emissions. Analysis of impact products, however, has the potential to provide useful information about planetary rings and small solar system bodies, such as asteroids and comets. Understanding the plasma dynamics and radiation mechanism is essential to addressing the impact threat and extracting science data from impacts. Charge attachment to condensed-phase debris may lead to a dusty plasma under certain conditions, so interpreting hypervelocity impacts requires knowledge of both the nature of the plasma and of the ejecta. We address the latter with measurements of the microscopic ejecta distribution produced by light gas gun impacts on solid aluminum and powdered regolith simulant targets. We examine both the size and shape of the ejecta using thin-film witness plates and find that the size distributions of microscopic ejecta follow power laws. Observations from the powdered regolith simulant match well with disruption experiments of solid basalt, while measurements from the aluminum impacts diverge from extrapolations based on studies of macroscopic debris. Analysis of the ejecta shape shows a transition from smooth to irregularly shaped ejecta at the material grain size, and the shape of debris may provide insight on the phase of the ejected material. Based on our results, we predict a

*Corresponding author
Email addresses: shohet@stanford.edu (Gil Shohet), bestacio@stanford.edu (Benjamin Estacio), imatt2@stanford.edu (Isaac Matthews), saqyoung@stanford.edu (Sean A. Q. Young), nnlee@stanford.edu (Nicolas Lee), sigridc@stanford.edu (Sigrid Close)

significant number of secondary impacts on plasma sensors due to ejecta, even at considerable distance from the target, supporting the hypothesis that charged dust affects plasma measurements in the ejecta curtain.

Keywords: Hypervelocity impact plasma, Ejecta characterization, Particle size distribution, Meteoroids, Space debris

---

1. Introduction

Meteoroids and dust routinely bombard bodies in space, such as spacecraft, asteroids, comets, and airless moons. Spacecraft in Earth orbit face the additional threat of impacts by orbital debris. These impacts, which occur at relative velocities ranging from a few to tens of km/s [1], are termed hypervelocity because the impact speeds are far greater than the acoustic speed in the impactor and target materials, resulting in hydrodynamic behavior. Impact events cause cratering or penetration of the target material, and generate an expanding plume of partially ionized plasma and macroscopic condensed phase ejecta. The risk of mechanical damage due to impact is well-established [2, 3], and mitigation strategies exist, including thin metal "Whipple" shields [4] and composite sandwich panels [5]. Unexplained spacecraft anomalies during periods of high meteoroid flux [6, 7, 8, 9] suggest an addtional threat of electrical damage. Even impacting particles too small to cause mechanical harm pose a threat because damage may occur due to radio frequency emissions and a broadband electromagnetic pulse produced by the impact plasma [10, 11, 12]. In-situ analysis of charged products from meteoroid impacts on small solar system bodies, however, may enable indirect surface characterization [13].

Detections of impact-generated plasma date back over half a century [14], and experimental observations include direct measurements [15, 16, 17, 18, 19], optical diagnostics [20, 21, 22, 23], and radio frequency measurements [11, 18, 24, 25]. Crawford and Schultz first described the impact plasma as "dusty" over thirty years ago [26], and charged dust has been proposed as a source of macroscopic charge separation and long-range electric fields, as well as a direct threat to electronics [10, 16, 27]. Dust production and charging in the context of impact plasmas, however, is poorly understood,

especially for spacecraft materials, such as aluminum. In particular, a rigorous study of dust charging in hypervelocity impacts requires knowledge of the size distribution of microscopic particles, which are more numerous and expected to carry the bulk of the attached charge.

Previous studies have employed a number of techniques to characterize the properties of ejecta from hypervelocity impacts, including particle collection, analysis of secondary impacts, and optical methods. Collection methods include capturing particles in media, such as foams or petroleum jelly [28, 29], and collection of ejecta from the impact chamber [30, 31, 32]. Capture methods have the advantage of allowing measurement of sub-micron ejecta, whereas post-impact collection is generally limited to particles a few hundred microns or larger; the capture medium, however, must be dissolved to extract the debris. Both these methods allow analysis of the fragment shape in addition to the particle size distribution [30, 31, 33]. Alternatively, ejecta may be characterized via secondary impacts, either by analyzing impact craters on polished metal or glass plates [5, 20, 28, 30, 34], or by measuring holes in thin membranes made from metal foils or plastics [35, 36, 37]. The mapping of impactor size to crater or hole size depends on the impactor velocity, ratio of particle size to target thickness, and target material properties [38]. Secondary impacts, however, can provide insight into both particle size and velocity, and allow characterization of ejecta on the order of a micron [35]. Optical methods, such as high-speed imaging, allow non-invasive study of the time-evolution of the ejecta cloud [20, 29, 39]. The size, velocity, and ejection time of individual particles may also be studied using laser illumination [40].

Studies of the ejecta size distribution typically fit the cumulative distribution of particles to a power law [41]

$$N(>d) = Cd^{-D}, \tag{1}$$

where $N(>d)$ is the number of particles with diameter greater than d, C is a constant, and D is the power law exponent. The majority of studies have focused on geologic and planetary materials, such as basalt [28, 35, 42, 43, 44], alumina [44], diorite [45], and sandstone [29]. A limited number of studies have examined ejecta from impacts on spacecraft materials or aluminum targets [32, 34, 46, 47]. Analysis by Buhl et al. [29]

found that the value of D depends on the specific energy of impact Q, defined as the ratio of impactor kinetic energy to target mass, relative to the critical value Q^*. When $Q > Q^*$, critical disruption occurs, as defined by the largest remaining target fragment containing no more than half the initial target mass. For semi-infinite geologic targets, $D \sim 2.5$ independent of impact velocity, whereas for disruption experiments, D is roughly a linear function of $\ln(Q/Q^*)$, with D-values in the range $1.44-3.26$ reported in the literature [29]. The NASA breakup model suggests $D = 1.71$ for aluminum impacts [46]. An aluminum-on-aluminum impact campaign by Nishida et al. [32], however, showed better agreement across a range of projectile masses and velocities with a bilinear exponential fit of the form

$$N(>d)/V^{1.5} = A_1 \exp\left(-B_1 d/d_p\right) + A_2 \exp\left(-B_2 d/d_p\right), \tag{2}$$

where V is the projectile velocity and d_p is the projectile diameter.

In this work, we present measurements of the size and shape of ejecta created by aluminum projectiles impacting aluminum and powdered regolith targets, which we use as analogues for spacecraft and small astronomical bodies, respectively. A number of studies have examined the size distribution of micron-scale ejecta for geologic and planetary materials, but to date no such data exist for impacts on spacecraft materials, such as aluminum. Moreover, to our knowledge, the shape of microscopic ejecta, which may have important implications for ejecta dynamics [48], has not previously been studied. We attempt to fill in these gaps using a thin polyester (PET) film witness plate design similar to [35] to characterize ejecta in the range of roughly $1-100$ μm in diameter. In Section 2 we describe the experiment and data analysis methodology. In Section 3 we present the computed particle size and ejecta shape distributions and compare to the literature. Finally, in Section 4, we discuss the implications of our results for both ground-based studies and hypervelocity impacts on spacecraft and other bodies, with an emphasis on the potential for ejecta charging and dusty plasma effects.

2. Methodology

2.1. Overview of experiment

In early 2019, we conducted an impact campaign at the NASA Ames Vertical Gun Range (AVGR), a two stage light gas gun that fires projectiles at hypervelocity speeds into a 2.5 m diameter vacuum chamber evacuated to a background pressure of approximately 0.5 Torr. In addition to the witness plates used for ejecta characterization, the sensor suite included Faraday cup plasma sensors, radio frequency antennas, photomultiplier tubes and photodiodes, and high speed cameras (Figure 1). We positioned plasma sensors and witness plates at elevation angles of 10°, 30°, 60°, and 90° from the chamber floor. To minimize interference with the expanding plasma and allow cameras and optical diagnostics a clear view, the plasma sensors and witness plates were mounted along two planes, one parallel and one perpendicular to the target surface. The upper plane was covered in a conductive mesh sharing a common ground with the sensor electronics to provide a clean electrical environment and reduce noise. A high-voltage power supply below the target assembly allowed biasing the target to between −300 V and +300 V relative to the chamber. The distance from target to the sensors was approximately 1 m, but varied slightly due to this geometry.

We shot a total of 13 targets of a variety of materials of interest to space applications, including 6061-T6 aluminum, copper, tungsten, FR-4 composite, glass, and a powdered regolith simulant comprised of a 50/50 mixture by weight of powdered dolomite and azomite. We compacted and baked the regolith simulant prior to shooting to prevent trapped moisture from disturbing the target surface during vacuum pump-down. All shots used 1.6 mm diameter (6 mg) spherical aluminum projectiles fired vertically and impacting the target at normal incidence. The impact velocities ranged from 4.38 to 5.88 km/s and impact parameters are tabulated in Table 1. See [27] for more details on the plasma sensor design and associated results.

The witness plate design is based on Nakamura et al. [35], where ejecta were characterized by counting holes due to secondary impacts on thin membranes of various thicknesses and materials. We chose PET film (Mylar) for the witness plates for two reasons. First, it is inexpensive and readily available in many micron-scale thicknesses.

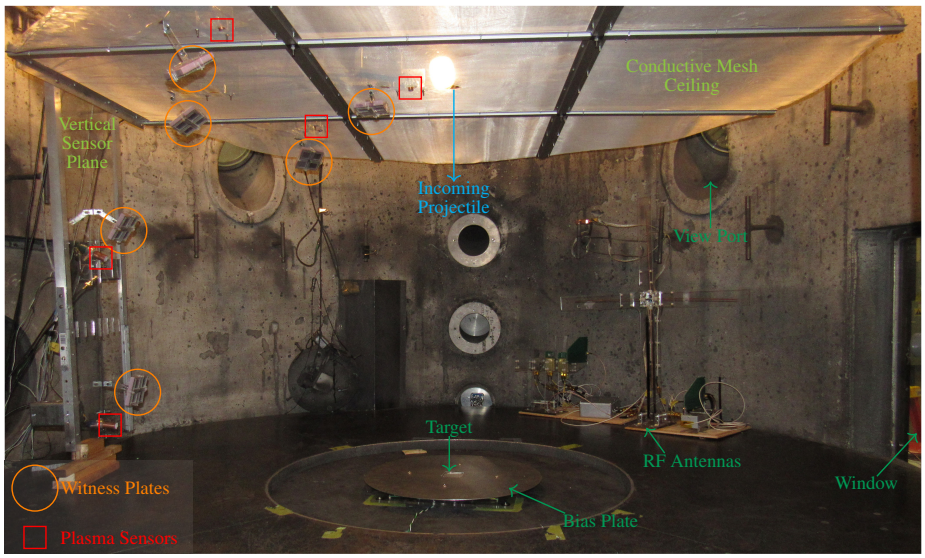

Figure 1: Interior of AVGR test chamber annotated with positions of sensors, target assembly, mounting structures, and path of incoming projectile. Plasma sensors (red squares) and witness plates (orange circles) were located at four elevation angles and two azimuthal positions. Optical instruments (not visible) were positioned in the test chamber window and view ports.

Second, the low yield strength compared with metal foils makes plastic film ideal for characterizing microscopic ejecta because the minimum ejecta size for penetration is reduced and, for ultra-thin films, the hole size closely approximates the impacting particle [35, 38].

Each witness plate consists of a sheet of film sandwiched between a laser-cut acrylic aperture, approximately 2.5 cm square, and a layer of polyethylene mesh to provide structural integrity. An assembly unit, shown in Figure 2, consists of four witness plates of different thickness PET film from 1 μm to 15 μm, a foam backing to prevent ricochet impacts, and a mounting structure designed for easy swapping of witness plates between shots. We used multiple thicknesses of film with the goal of estimating ejecta velocity based on differential penetration of different thickness films. Due to the distance of the witness plates from the impact site, however, there were insufficient secondary impacts to enable velocity estimates. We present ejecta size and shape measurements from the 1 μm thick films to minimize the error incurred by assuming the

Shot	Material	Target Bias (V)	Impact Speed (km/s)
1	Al	0	4.38
2	Al	0	5.38
3	Al	+50	5.88
4	Al	+300	5.19
5	Al	−50	4.97
6	Al	−100	5.38
7	Al	−300	5.41
8	Cu	0	5.09
9	W	0	5.46
10	Al	−300	5.44
11	FR-4	0	5.66
12	Regolith Simulant	0	5.56
13	Glass	0	5.59

Table 1: Summary of target configurations and impact speeds.

hole profile approximately matches the ejecta profile.

2.2. Data analysis

We imaged the witness plates using a digital camera mounted in the trinocular port of a polarizing microscope equipped with a 20x objective lens with numerical aperture of 0.45. Based on the diffraction limit, this configuration can theoretically resolve features as small as approximately 0.7 μm, although differentiating holes from optical artifacts and obtaining accurate measurements is difficult near the diffraction limit. We imaged a subset of the surface by taking approximately 700 photographs of each witness plate analyzed. To prevent repeated counts and obtain as complete a sample as possible, we imaged each witness plate in a single session taking care to advance the microscope table sufficiently between images to avoid overlap. The optical configuration resulted in vignetting, with each image containing a vignette circle approximately 580 μm in diameter. In practice, a circular region about 480 μm in diameter is sufficiently well-focused to reliably identify holes. After processing, the total area analyzed for hole counting purposes corresponds to approximately 20% of the unobstructed surface of each witness plate.

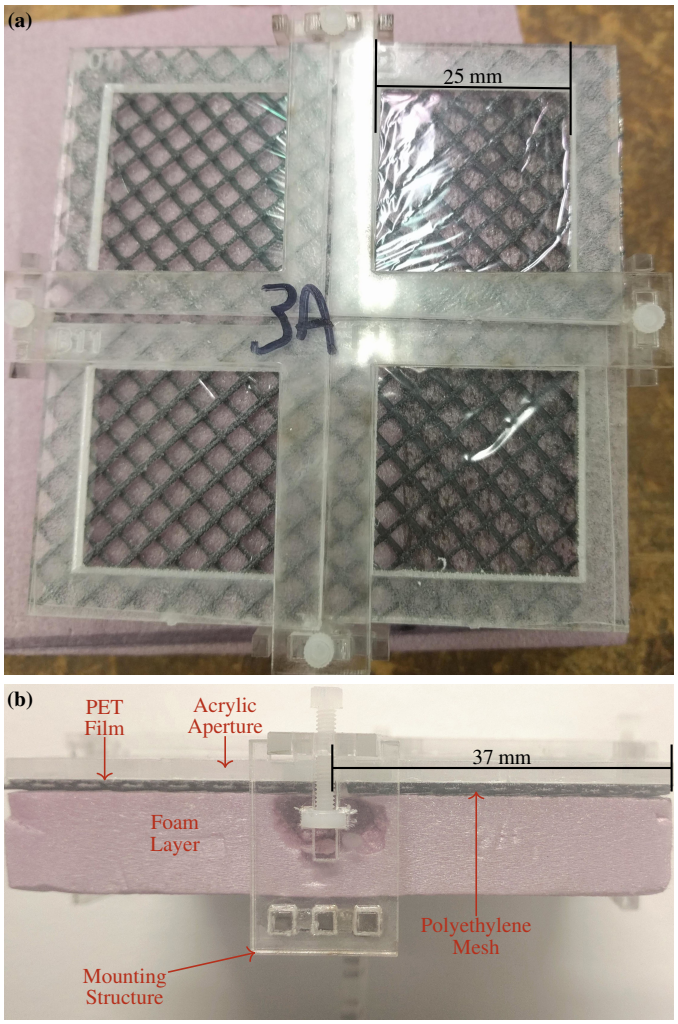

Figure 2: **(a)** Top view of the witness plate assembly. Each aperture contains a different thickness of PET film. **(b)** Side view of the witness plate annotated with the assembly components.

We processed and analyzed the images using OpenCV with a combination of automated pre-processing and manual hole identification. We first pre-processed the images using a simple algorithm that identifies the vignette circle and well-focused region via thresholding, crops images to the vignette circle, and improves clarity by aligning the color channels to correct for errors introduced by the optical apparatus and camera sensor. Automated hole identification proved unreliable, so we manually identified holes

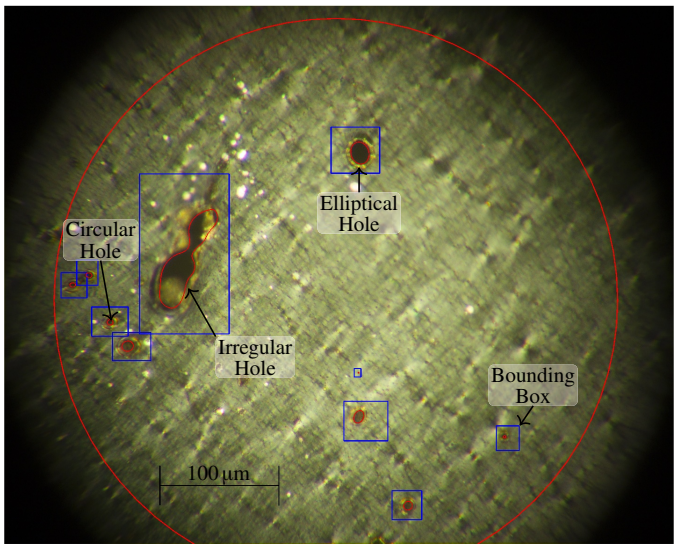

Figure 3: Witness plate micro-photograph with holes identified and outlined. We note representative examples of a circular, elliptical, and irregularly shaped hole, as well as the bounding boxes used in identifying holes for measurement. The red circle indicates the boundary of the well-focused region, inside of which we search for holes.

in each image, defining a bounding box around each hole. Finally, we measured the area of each hole, in pixels, by magnifying the bounding box regions, identifying points on the boundary, and fitting a bounded curve. We fit circular and elliptical holes using a least-squares method, and irregularly-shaped holes using closed cubic spline curves. Figure 3 shows a processed micro-photograph with holes identified. We converted pixel measurements to real units by calibration against an object of known size.

A rigorous discussion and quantification of error sources and uncertainties is lacking in many studies. In this study we attempted to quantify uncertainties to the greatest extent possible, and to propagate these errors in our estimates of the particle size distribution. First, we made multiple calibration measurements, and found a minor uncertainty ($<1\%$) in the conversion from pixels to real units. Second, by analyzing a subset of 100 images from each witness plate over five independent trials, we built an uncertainty model to account for human error in hole identification and measurement. Third, we found a systematic undercount of small holes near the boundaries of the vignette

circles due to variable focus and brightness in the images.

We account for the measurement uncertainties by treating each measured hole area as an independent random variable and resampling the areas of all measured holes over 10,000 independent trials. During each trial, we first resample the pixel to real unit conversion based on the calibration uncertainty, and then account for human error by independently resampling the size of each hole assuming the relative error is a Gaussian random variable with variance $\sigma^2(A) = \sigma_{\mathrm{m}}^2(A) + \sigma_{\mathrm{id}}^2$. The relative measurement uncertainty $\sigma_{\mathrm{m}}(A)$ depends on the area because an equivalent absolute error results in a larger relative error in small holes compared to large holes. In practice, a constant relative error term σ_{id} well approximates the uncertainty due to human error identifying holes. After resampling, we apply a correction to each trial to conservatively correct for the under-counting.

In addition to the aforementioned errors, the cumulative distribution suffers from finite count effects, with small number statistics especially important for large holes. Given a set of holes with areas $\{A\}_i$ corresponding to trial i from the resampled data, the number of holes with area greater than A is $N_i(>A)$. We model $N(>A)$, the true count of holes with area greater than A, as a Poisson-like process, allowed to be continuous for numerical reasons. Under these assumptions, if we apply the Bayes theorem with a uniform prior, the number of holes with area greater than A is a random variable with cumulative distribution [49]

$$F_i(x, N_i(>A)) = \frac{\Gamma(x, N_i)}{\Gamma(x)} \tag{3}$$

where $\Gamma(x)$ is the gamma function and $\Gamma(x, N_i(>A))$ is the upper incomplete gamma function. By linearity, averaging over the $M = 10000$ independent trials, the cumulative distribution of $N(>A)$ is estimated by $F(x) = \frac{1}{M}\sum_{i=1}^{M} F_i(x, N_i(>A))$. Finally, we numerically invert F to obtain an estimate for $N(>A)$ and associated uncertainty band for a given hole area A.

Beyond the error sources we are able to quantify, there are some sources we were unable to model explicitly. For example, the assumption of the hole size being equal to the incoming ejecta may be violated for particles approaching the film thickness. Quantifying this error is difficult, however, without an accurate material model and

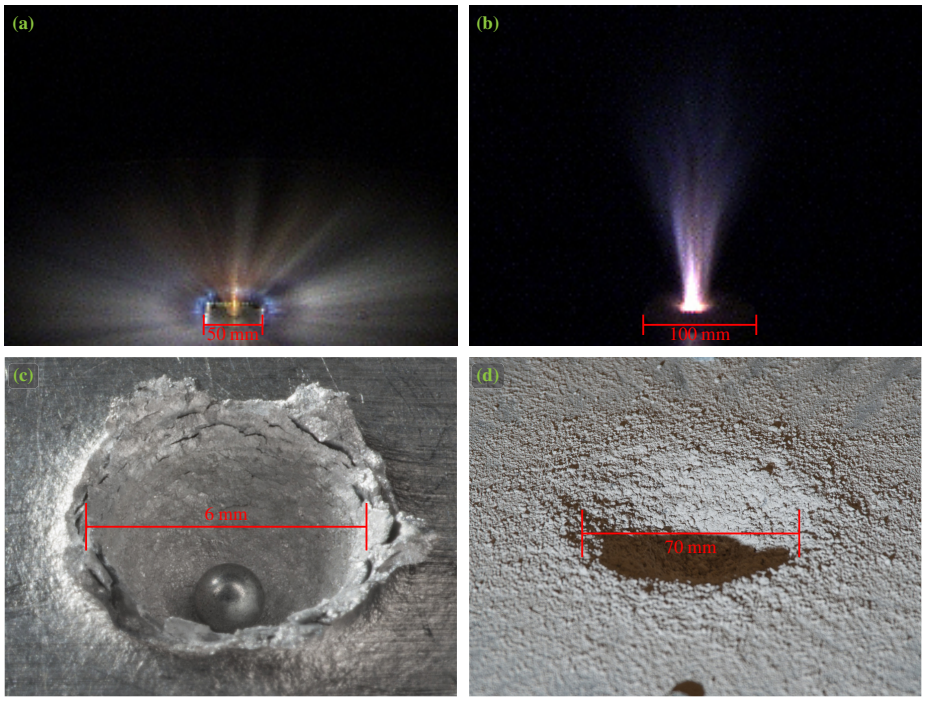

Figure 4: **(a)** High speed video still of the impact flash from an aluminum-on-aluminum impact. **(b)** High speed video still from the impact on the powdered regolith simulant. **(c)** Impact crater on an aluminum target with the 1.6 mm diameter projectile placed in the crater for reference. **(d)** Impact crater in the powdered regolith simulant.

knowledge of the velocities of the microscopic ejecta. Moreover, individual witness plates only cover a small portion of the ejecta cone, so spatial variations in the ejecta density may influence results. Nevertheless, such errors plague virtually every study, and we do not expect excessive influence on the overall nature of the results.

3. Results & Discussion

In practice, the targets were insufficiently large to prevent wave reflection off the target boundaries during the impact process, but were sufficient in size to preclude destruction. Only a small percentage of the initial target mass was ejected during impact, and impacts did not visibly affect the edges or underside of the aluminum and regolith simulant targets. Figure 4 shows high speed video stills and impact craters from im-

pacts on aluminum and powdered regolith simulant. For the aluminum impacts, ejecta were concentrated in a narrow band approximately 60° from the ground plane, and the 1.6 mm diameter projectile produced a crater roughly 6 mm in diameter. In contrast, the regolith target produced a much larger impact crater roughly 70 mm in diameter, and the ejecta were concentrated in a cone around the vertical. We also observed evidence of charged dust in plasma sensor readings at positions corresponding to the respective ejecta curtains of both materials [27].

We were only able to obtain sufficient hole counts directly in the path of the primary ejecta curtain because the witness plates were located a significant distance away from the target to avoid interference with other diagnostics. Moreover, because the metal targets produced considerably less ejecta than the powdered regolith simulant, we found that a single impact produced insufficient ejecta to obtain statistically significant counts. Therefore, for the aluminum impacts we present integrated and averaged results where the witness plate was left in the test chamber for three shots. The three impacts on the aluminum targets occurred at 4.97, 5.38, and 5.41 km/s, and the regolith simulant impact occurred at 5.56 km/s. For the impacts on aluminum targets we present results from the 1 μm thick witness plate located at 60° from the ground plane. For the regolith simulant impact we present results from the 1 μm thick witness plate located directly above the target.

3.1. Ejecta size distributions

We present the solid-angle normalized ejecta size distributions for the regolith simulant and aluminum impacts in Figures 6 and 7, respectively. We limit our analysis to holes at least 1 μm in diameter because the assumption of the hole cross-section matching that of the particle is violated for particles smaller than the film thickness and measuring holes reliably becomes difficult near the diffraction limit. We present results in the form of the cumulative distribution $n(>A)$, defined as the solid-angle-normalized number of particles producing holes with cross-sectional area greater than A. For comparison with the literature, we define the equivalent diameter d_{eq} such that $\pi d_{\mathrm{eq}}^2/4 = A$, and we recast the power law (1) as $n(>A) \propto A^{-D/2}$ to compare our results with D-values from previous studies.

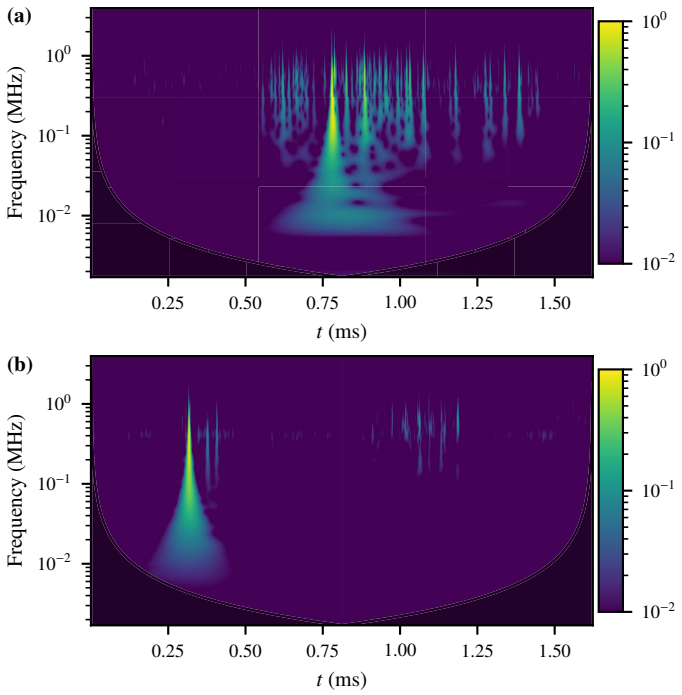

Figure 5: Wavelet transforms of Faraday cup plasma measurements from sensors located in the ejecta curtain. **(a)** Regolith simulant impact (90° from the horizontal). **(b)** Aluminum impact (60° from the horizontal). Thin vertical bands indicate impulsive observations, which likely correspond to dust detections due to secondary impacts by charged ejecta. The magnitudes are normalized by the maximum value observed for each shot.

Based on our measurements, we also compute the expected cumulative number of detections for a plasma sensor with cross-section 1.6 mm^2. For the co-located plasma sensor, we predict approximately 250 secondary impacts by ejecta at least 1μm in diameter for the regolith simulant impact, and approximately 25 for the aluminum impacts. To compare with plasma measurements, we processed the filtered Faraday cup data with a continuous wavelet transform using Morlet wavelets [50] with non-dimensional frequency $\omega_0 = 6$. Secondary impacts by charged dust deposit their charge on a time scale much faster than the plasma sensor response time and are detected as impulses. Such impulses in the plasma data manifest as thin vertical bands in Figure 5, which shows the wavelet-transformed data for the regolith simulant impact and one representative aluminum impact. We found order of magnitude agreement with predicted dust

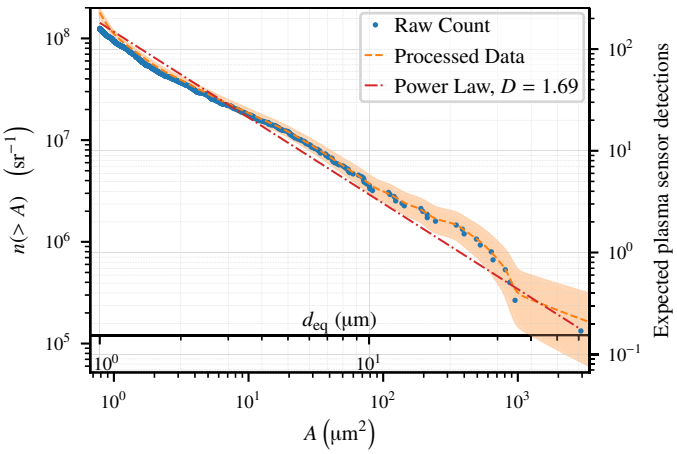

Figure 6: Solid-angle normalized particle size distribution for the powdered regolith simulant impact. Blue dots show the raw measurements. The orange line indicates the estimated distribution after resampling using the uncertainty model, applying corrections, and accounting for finite-count effects, with the shaded region indicating the 1-σ uncertainty band. The dashed-dotted red line shows the best fit D-value of 1.69.

impacts, counting approximately 5−10 such bands in a given aluminum impact, and approximately 40−50 from the regolith simulant impact. The discrepancy from the prediction may simply be due to spatial variations, but the difference suggests ejecta smaller than approximately 2−3 μm may not be detectable by the plasma sensors used in the experiment.

The predicted particle flux to a sensor in the regolith simulant ejecta curtain is only 10 times greater than the predicted flux to a sensor in the aluminum ejecta curtain, despite the regolith simulant ejecting 400 times the material by mass. This is because the aluminum debris are concentrated in a much narrower band than the regolith ejecta. Based on the trend observed we predict a larger number of secondary impacts by particles on the order of ∼0.5−1 μm. A basic drag analysis, however, suggests the 0.5 Torr neutral background in the test chamber will prevent particles much smaller than 0.5 μm from reaching the sensors, and the plasma may also ablate these nano-scale particles.

For the impact on the regolith simulant, after data processing and uncertainty analysis, we computed $D = 1.69^{+0.04}_{-0.03}$. After impact, we found a net change in the target mass of 14 g, or 3.3% of the initial 420 g. Most hypervelocity impact studies on planetary

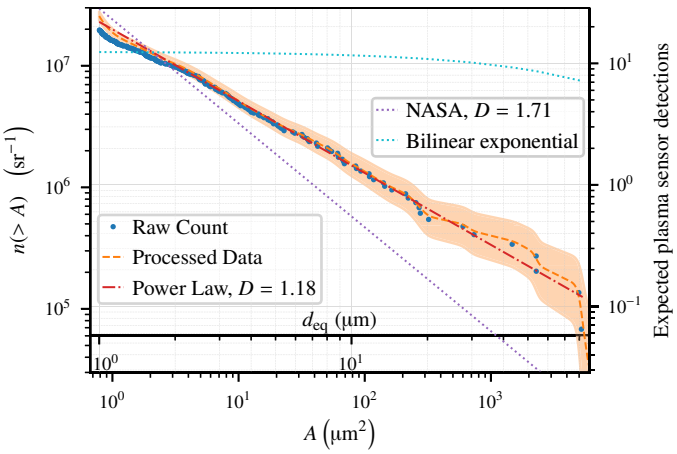

Figure 7: Solid-angle normalized particle size distribution for the aluminum impacts. Blue dots show the raw measurements. The orange line indicates the estimated distribution after resampling using the uncertainty model, applying corrections, and accounting for finite-count effects, with the shaded region indicating the 1-σ uncertainty band. The dash-dotted red line shows the best fit D-value of 1.18. Fitting to the NASA breakup model [46] D-value of D = 1.71 (dotted purple), overestimates the relative abundance of fine ejecta. Fitting to the bilinear exponential with exponent values proposed by Nishida et al. [32] (dotted cyan), significantly underestimates the relative abundance of fine ejecta.

materials have observed larger D-values, but the value does fall in the range observed for impacts on basalt slightly below the critical specific energy [29, 43, 51]. It is unclear how to define a critical specific energy for a powdered target, but the specific impact energy of $Q = 0.22$ falls in the transition range where targets are neither semi-infinite nor completely destroyed. Previous studies of other materials show D-values of 1.5−2.0 in that regime. Of course, for the powdered target, the level of compaction and pre-impact grain size distribution likely play major roles in determining the ejecta properties. For ejecta 1−50 μm in diameter, the measured quantity per solid angle agrees well with disruption experiments of basalt with normal impact angle [35].

For the aluminum impacts, the observed cratering is in good agreement with previous experiments, e.g. [32]. The average quantity of material ejected was 43 mg, about 7 times the projectile mass and 0.07 % of the target mass. Our results support the observation by Nishida et al. [32] that the NASA breakup model [46] significantly overestimates the relative abundance of ejecta below a certain size. We found, however,

the bilinear exponential form used by Nishida et al. for macroscopic ejecta was also poor fit to our data, significantly underestimating the relative abundance of microscopic particles. We found a power law to be the best fit to the data and, after data processing and uncertainty analysis, computed $D = 1.18^{+0.10}_{-0.07}$. Note that the smallest particles measured by Nishida et al. (~500 μm) are larger than the largest ejecta we recorded (~100 μm), and further study is needed to patch the transition between macroscopic debris visible to the naked eye and microscopic debris on the order of or smaller than the material grain size.

3.2. Ejecta shape

We use two simple metrics to characterize the shape of debris particles. For a hole with area A and perimeter P, we define a simple, dimensionless circularity metric $4\pi A/P^2$, which is unity for a circle and less than one for any other shape. For comparison with the results of Nishida et al. [30] examining macroscopic ejecta from aluminum targets, we also consider the axis ratio b/a, where a is the major axis and b is the minor axis. For irregularly shaped holes, we compute b/a based on the axis ratio of the best fit ellipse. In Figure 8, we show the circularity metric versus hole area and in Figure 9 the cumulative distribution of axis ratios, $N(\geq b/a)$, defined as the number of holes with axis ratio at least b/a. We find that secondary impacts from larger particles result in holes with less circular and more irregular cross sections. Note in practice we generally classified holes with $d_{\mathrm{eq}} \lesssim 1.5$ μm as circular because it is difficult to resolve the shape near the diffraction limit, but the trend for holes larger than approximately 2 μm is clear. We considered the possibility of irregular holes resulting from multiple overlapping secondary impacts, but at the ~1 m distance, the ejecta density is sufficiently small that overlapping impacts are improbable.

The regolith simulant impact shows a more obvious trend towards less circular ejecta for $d_{\mathrm{eq}} \gtrsim 3$ μm compared with the aluminum impact, where there is a mixture of nearly circular and highly irregular ejecta for the range of $2 \lesssim d_{\mathrm{eq}} \lesssim 15$ μm. In agreement with [30], we find that the bulk of aluminum debris have $0.8 \lesssim b/a \lesssim 0.95$, in contrast to the regolith ejecta, where the distribution of axis ratios is more uniform. Holes with cross-sectional area $A \gtrsim 100$ μm^2 are predominantly irregular in shape for

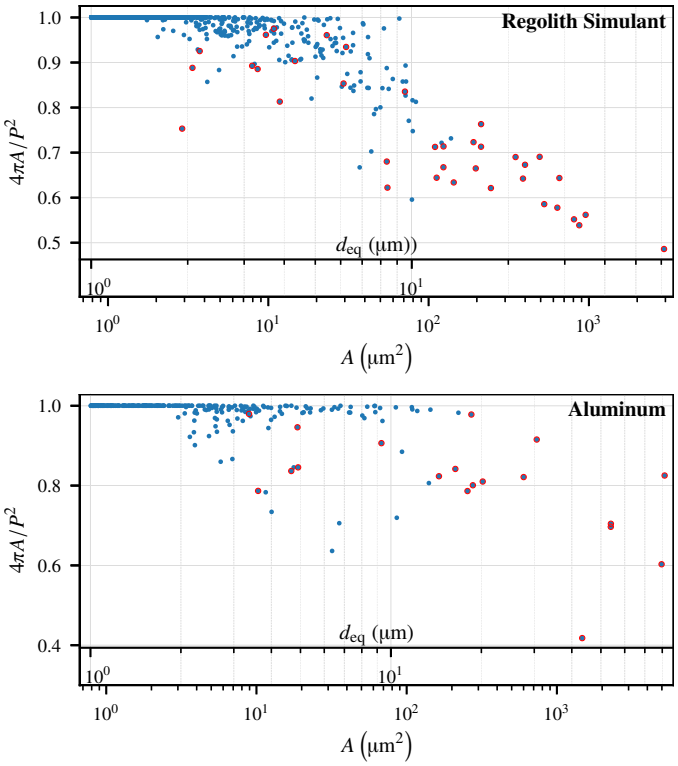

Figure 8: Hole circularity metric versus hole size for the regolith simulant and aluminum impacts. A red outline indicates the hole is irregularly shaped.

both the regolith simulant and aluminum impacts.

A key question is whether we can glean anything about the material phase based on the shape of ejecta. Highly non-circular or irregular ejecta likely correspond to solid material ejected from the impact crater, and particles that produce smooth, nearly circular cross-sections more likely correspond to material ejected as liquid-phase droplets. Possibly due to aluminum fragments on the order of the material grain size having highly irregular shapes, a larger proportion of ejecta from the aluminum impact made irregular impressions compared with ejecta from the regolith simulant impact. At the same time, the impact process in solid aluminum produces a larger fraction of molten material. We suspect the existence of a significant population of nearly spherical ejecta up to almost 20 μm in diameter is due to liquid droplets ejected from the aluminum

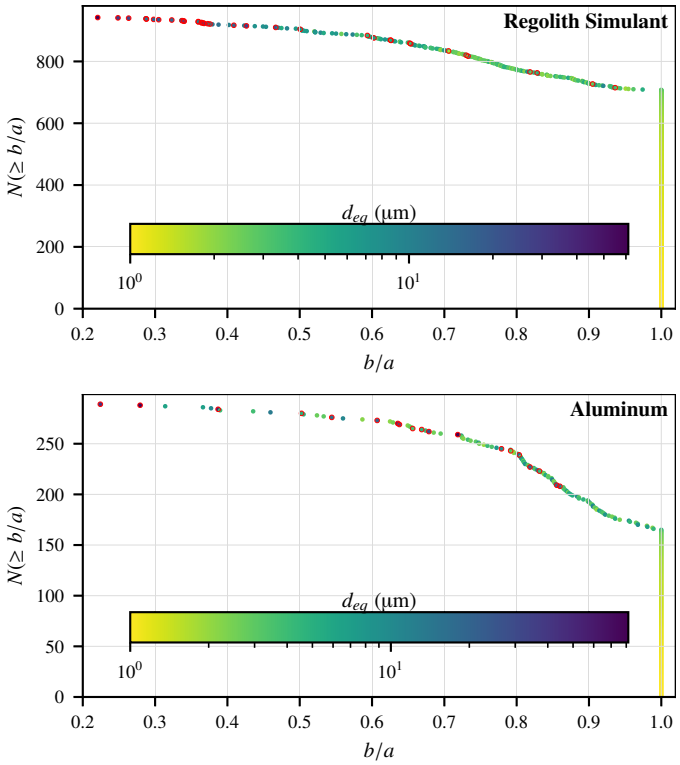

Figure 9: Cumulative distribution of minor-to-major axis ratios of holes due to debris from the regolith simulant and aluminum impacts. Points are shaded by equivalent diameter, d_{eq}, and a red outline indicates an irregularly shaped hole.

target. Drawing such conclusions for the regolith simulant impact is more difficult because the target is composed of a granular medium. A large volume of solid particles is ejected on impact and observations depend strongly on the initial target composition.

4. Conclusions

Using observations from 1 μm thick PET film witness plates, we computed the particle size distributions for microscopic ejecta produced by hypervelocity light gas gun impacts on the order of 5 km/s into powdered regolith simulant and solid aluminum targets. We found the particle size distribution for the regolith simulant target followed a power law with D-value of 1.69. Both the power law scaling and solid angle normal-

ized ejecta density from the powdered regolith simulant are in reasonable agreement with results from disruption studies on solid basalt, despite the material properties differing greatly. To our knowledge, no previous study has attempted to characterize the micron-scale ejecta from an aluminum-on-aluminum impact, and we found a D-value of 1.18. Our results suggest the relative abundance of microscopic ejecta is underestimated by debris measurements by Nishida et al. [32] of millimeter-scale debris, and overestimated by the NASA breakup model [46].

By examining the cross-section of the holes produced by secondary impacts, we also analyzed the shape of microscopic debris, to our knowledge the first analysis of this sort. For both impacts, we observed a transition with increasing ejecta size from circular or nearly circular holes to more eccentric and irregular shapes. Ejecta cross-sections may provide information about the phase of the material, with microscopic material ejected in the liquid phase being more uniform compared with solid fragments on the order of the material grain size. Given that the shape of the ejecta can have important implications for the particle dynamics in rarefied gas environments, such as those found in ground-based facilities and around outgassing comets, this warrants further study.

Our analysis suggests that plasma sensors in the path of the ejecta curtain will observe a significant number of impacts by microscopic debris. Indeed, the number of impulsive detections, which are indicative of charged dust, agrees in order of magnitude with the predicted flux. These observations lend support to the hypothesis that dust-plasma interactions play an important role in hypervelocity impacts, at least in the impactor mass and velocity regime attainable in light gas gun facilities. This has implications for understanding the impact threat to satellites and for analyzing impact events on small solar system bodies, as the dust component must be taken into account depending on the impact conditions and materials involved. Most meteoroid impacts occur with higher velocities and smaller masses than those attainable in light gas gun facilities, resulting in a larger fraction of ionized material and less debris. More study is needed to determine the mass, velocity, and material regimes in which ejecta charging is significant. Going forward, we plan to combine the plasma and ejecta observations with dust charging and dynamics models to make quantitative estimates of post-impact

dust charging under light gas gun conditions and examine how the neutral background affects observations.

Acknowledgements

This work is supported by AFOSR grant FA9550-14-1-0290. Work by G. Shohet is supported by the DOE NNSA Stewardship Science Graduate Fellowship grant DE-NA0003960. We would also like to thank all of the AVGR staff for their invaluable support in performing the impact campaign.

References

[1] P. Brown, R. E. Spalding, D. O. ReVelle, E. Tagliaferri, S. P. Worden, The flux of small near-Earth objects colliding with the Earth, Nature 420 (6913) (2002) 294–296. doi:10.1038/nature01238.

[2] R. L. Bjork, K. N. Kreyenhagen, M. H. Wagner, Analytical Study of Impact Effects as Applied to the Meteoroid Hazard, National Aeronautics and Space Administration, 1967.

[3] B. G. Cour-Palais, Hypervelocity impact in metals, glass and composites, International Journal of Impact Engineering 5 (1) (1987) 221–237. doi:10.1016/0734-743X(87)90040-6.

[4] F. L. Whipple, Meteorites and space travel., The Astronomical Journal 52 (1947) 131. doi:10.1086/106009.

[5] S. Ryan, F. Schaefer, R. Destefanis, M. Lambert, A ballistic limit equation for hypervelocity impacts on composite honeycomb sandwich panel satellite structures, Advances in Space Research 41 (7) (2008) 1152–1166. doi:10.1016/j.asr.2007.02.032.

[6] R. D. Caswell, N. McBride, A. Taylor, Olympus end of life anomaly — a perseid meteoroid impact event?, International Journal of Impact Engineering 17 (1) (1995) 139–150. doi:10.1016/0734-743X(95)99843-G.

[7] J. A. M. McDonnell, N. McBride, D. J. Gardner, The Leonid Meteoroid Stream: Spacecraft Interactions and Effects, Second European Conference on Space Debris 393 (1997) 391.

[8] N. McBride, J. a m McDonnell, Meteoroid impacts on spacecraft:: Sporadics, streams, and the 1999 Leonids, Planetary and Space Science 47 (8) (1999) 1005–1013. doi:10.1016/S0032-0633(99)00023-9.

[9] A. Goel, S. Close, Electrical anomalies on spacecraft due to hypervelocity impacts, 2015 IEEE Aerospace Conference (2015) 1–7doi:10.1109/AERO.2015.7119039.

[10] S. Close, P. Colestock, L. Cox, M. Kelley, N. Lee, Electromagnetic pulses generated by meteoroid impacts on spacecraft, Journal of Geophysical Research: Space Physics 115 (A12) (Dec. 2010). doi:10.1029/2010JA015921.

[11] S. Close, I. Linscott, N. Lee, T. Johnson, D. Strauss, A. Goel, A. Fletcher, D. Lauben, R. Srama, A. Mocker, S. Bugiel, Detection of electromagnetic pulses produced by hypervelocity micro particle impact plasmas, Physics of Plasmas 20 (9) (2013) 092102. doi:10.1063/1.4819777.

[12] A. C. Fletcher, S. Close, Particle-in-cell simulations of an RF emission mechanism associated with hypervelocity impact plasmas, Physics of Plasmas 24 (5) (2017) 053102. doi:10.1063/1.4980833.

[13] N. Lee, S. Close, Meteoroid Impact Detection for Exploration of Asteroids: Small Satellites for Asteroid Characterization, Journal of Spacecraft and Rockets 55 (1) (2017) 202–213. doi:10.2514/1.A33928.

[14] J. F. S. Friichtenicht, IONIZATION ASSOCIATED WITH HYPERVELOCITY IMPACT, Tech. Rep. NASA-TN-D-2091, NASA (Aug. 1963).

[15] P. R. Ratcliff, M. J. Burchell, M. J. Cole, T. W. Murphy, F. Alladfadi, Experimental measurements of hypervelocity impact plasma yield and energetics, International Journal of Impact Engineering 20 (6) (1997) 663–674. doi:10.1016/S0734-743X(97)87453-2.

[16] D. A. Crawford, P. H. Schultz, Electromagnetic properties of impact-generated plasma, vapor and debris, International Journal of Impact Engineering 23 (1, Part 1) (1999) 169–180. doi:10.1016/S0734-743X(99)00070-6.

[17] N. Lee, S. Close, D. Lauben, I. Linscott, A. Goel, T. Johnson, J. Yee, A. Fletcher, R. Srama, S. Bugiel, A. Mocker, P. Colestock, S. Green, Measurements of freely-expanding plasma from hypervelocity impacts, International Journal of Impact Engineering 44 (2012) 40–49. doi:10.1016/j.ijimpeng.2012.01.002.

[18] N. Lee, S. Close, A. Goel, D. Lauben, I. Linscott, T. Johnson, D. Strauss, S. Bugiel, A. Mocker, R. Srama, Theory and experiments characterizing hypervelocity impact plasmas on biased spacecraft materials, Physics of Plasmas 20 (3) (2013) 032901. doi:10.1063/1.4794331.

[19] P. Tarantino, A. Goel, A. Corso, N. Lee, S. Close, An electrostatic method to model the expansion of hypervelocity impact plasma on positively biased surfaces, Physics of Plasmas 25 (9) (2018) 092103. doi:10.1063/1.5039656.

[20] K. Weber, V. Hohler, A. J. Stilp, Impact flash and debris cloud expansion of high-pure metal foils, International Journal of Impact Engineering 14 (1) (1993) 797–808. doi:10.1016/0734-743X(93)90073-G.

[21] D. Heunoske, M. Schimmerohn, J. Osterholz, F. Schäfer, Time-resolved Emission Spectroscopy of Impact Plasma, Procedia Engineering 58 (2013) 624–633. doi:10.1016/j.proeng.2013.05.072.

[22] A. Goel, N. Lee, S. Close, Estimation of hypervelocity impact parameters from measurements of optical flash, International Journal of Impact Engineering 84 (2015) 54–63. doi:10.1016/j.ijimpeng.2015.05.008.

[23] Y. M. Hew, A. Goel, S. Close, N. Lee, Hypervelocity impact flash and plasma on electrically biased spacecraft surfaces, International Journal of Impact Engineering 121 (2018) 1–11. doi:10.1016/j.ijimpeng.2018.05.008.

[24] K. Maki, T. Takano, A. Fujiwara, A. Yamori, Radio-wave emission due to hypervelocity impacts in relation to optical observation and projectile speed, Advances

in Space Research 34 (5) (2004) 1085–1089. doi:10.1016/j.asr.2003.02.032.

[25] A. Nuttall, M. Kochenderfer, S. Close, Detection of hypervelocity impact radio frequency pulses through prior constrained source separation, Radio Science 51 (10) (2016) 1660–1675. doi:10.1002/2016RS006108.

[26] D. A. Crawford, P. H. Schultz, Laboratory observations of impact–generated magnetic fields, Nature 336 (1988) 50.

[27] B. Estacio, G. Shohet, S. A. Q. Young, I. Matthews, N. Lee, S. Close, Dust and atmospheric effects on light gas gun hypervelocity impact experiments, Preprint submitted to International Journal of Impact Engineering (May 2020).

[28] N. Asada, Fine fragments in high-velocity impact experiments, Journal of Geophysical Research: Solid Earth 90 (B14) (1985) 12445–12453. doi:10.1029/JB090iB14p12445.

[29] E. Buhl, F. Sommer, M. H. Poelchau, G. Dresen, T. Kenkmann, Ejecta from experimental impact craters: Particle size distribution and fragmentation energy, Icarus 237 (2014) 131–142. doi:10.1016/j.icarus.2014.04.039.

[30] M. Nishida, K. Hayashi, J. Nakagawa, Y. Ito, Influence of temperature on crater and ejecta size following hypervelocity impact of aluminum alloy spheres on thick aluminum alloy targets, International Journal of Impact Engineering 42 (2012) 37–47. doi:10.1016/j.ijimpeng.2011.11.006.

[31] T. Michikami, A. Hagermann, T. Kadokawa, A. Yoshida, A. Shimada, S. Hasegawa, A. Tsuchiyama, Fragment shapes in impact experiments ranging from cratering to catastrophic disruption, Icarus 264 (2016) 316–330. doi:10.1016/j.icarus.2015.09.038.

[32] M. Nishida, Y. Hiraiwa, K. Hayashi, S. Hasegawa, Scaling laws for size distribution of fragments resulting from hypervelocity impacts of aluminum alloy spherical projectiles on thick aluminum alloy targets: Effects of impact velocity

and projectile diameter, International Journal of Impact Engineering 109 (2017) 400–407. doi:10.1016/j.ijimpeng.2017.08.005.

[33] F. Sommer, F. Reiser, A. Dufresne, M. H. Poelchau, T. Hoerth, A. Deutsch, T. Kenkmann, K. Thoma, Ejection behavior characteristics in experimental cratering in sandstone targets, Meteoritics & Planetary Science 48 (1) (2013) 33–49. doi:10.1111/maps.12017.

[34] S. Masuyama, S. Matsumoto, P. Faure, H. Nakamoto, Y. Akahoshi, T. Koura, H. Matsumoto, Y. Kitazawa, Feasibility of Standardized Ejecta Evaluation for Spacecraft Surface Materials, Procedia Engineering 58 (2013) 543–549. doi:10.1016/j.proeng.2013.05.062.

[35] A. M. Nakamura, A. Fujiwara, T. Kadono, Velocity of finer fragments from impact, Planetary and Space Science 42 (12) (1994) 1043–1052. doi:10.1016/0032-0633(94)90005-1.

[36] S. Yamamoto, A. M. Nakamura, Velocity distribution of powdery ejecta, Advances in Space Research 20 (8) (1997) 1581–1584. doi:10.1016/S0273-1177(97)00815-6.

[37] J. M. Mihaly, J. D. Tandy, M. A. Adams, A. J. Rosakis, In situ diagnostics for a small-bore hypervelocity impact facility, International Journal of Impact Engineering 62 (2013) 13–26. doi:10.1016/j.ijimpeng.2013.05.004.

[38] F. Hörz, M. J. Cintala, R. P. Bernhard, T. H. See, Dimensionally scaled penetration experiments to extract projectile sizes from space exposed surfaces, International Journal of Impact Engineering 14 (1) (1993) 347–358. doi:10.1016/0734-743X(93)90033-4.

[39] A. J. Piekutowski, Characteristics of debris clouds produced by hypervelocity impact of aluminum spheres with thin aluminum plates, International Journal of Impact Engineering 14 (1) (1993) 573–586. doi:10.1016/0734-743X(93)90053-A.

[40] M. Schimmerohn, E. Watson, M. Gulde, L. Kortmann, F. Schäfer, Measuring ejecta characteristics and momentum transfer in experimental simulation of kinetic impact, Acta Astronautica (2018). doi:10.1016/j.actaastro.2018.01.046.

[41] D. L. Turcotte, Fractals and fragmentation, Journal of Geophysical Research: Solid Earth 91 (B2) (1986) 1921–1926. doi:10.1029/JB091iB02p01921.

[42] D. Gault, E. Shoemaker, H. Moore, U. S. N. Aeronautics, S. Administration, A. R. Center, Spray Ejected from the Lunar Surface by Meteoroid Impact, NASA Technical Note, National Aeronautics and Space Administration, 1963.

[43] Y. Takagi, H. Mizutani, S.-I. Kawakami, Impact fragmentation experiments of basalts and pyrophyllites, Icarus 59 (3) (1984) 462–477. doi:10.1016/0019-1035(84)90114-3.

[44] A. Nakamura, A. Fujiwara, Velocity distribution of fragments formed in a simulated collisional disruption, Icarus 92 (1) (1991) 132–146. doi:10.1016/0019-1035(91)90040-Z.

[45] M. J. Cintala, F. Horz, Catastrophic Rupture Experiments: Fragment-Size Analysis and Energy Considerations, LPI (1984) 158–159.

[46] N. L. Johnson, P. H. Krisko, J. C. Liou, P. D. Anz-Meador, NASA's new breakup model of evolve 4.0, Advances in Space Research 28 (9) (2001) 1377–1384. doi:10.1016/S0273-1177(01)00423-9.

[47] P. Faure, Y. Akahoshi, S. Masuyama, H. Nakamoto, K. Norimatsu, T. Koura, Normal and 45° Hypervelocity Impact Tests to Evaluate Spacecraft Material Ejecta, 6th European Conference on Space Debris 723 (2013) 111.

[48] S. L. Ivanovski, V. V. Zakharov, V. Della Corte, J.-F. Crifo, A. Rotundi, M. Fulle, Dynamics of aspherical dust grains in a cometary atmosphere: I. axially symmetric grains in a spherically symmetric atmosphere, Icarus 282 (2017) 333–350. doi:10.1016/j.icarus.2016.09.024.

[49] A. Ilienko, Continuous counterparts of Poisson and binomial distributions and their properties, arXiv:1303.5990 [math] (Mar. 2013). arXiv:1303.5990.

[50] C. Torrence, G. P. Compo, A Practical Guide to Wavelet Analysis, Bulletin of the American Meteorological Society 79 (1) (1998) 61–78. doi:10.1175/1520-0477(1998)079<0061:APGTWA>2.0.CO;2.

[51] A. Fujiwara, G. Kamimoto, A. Tsukamoto, Destruction of basaltic bodies by high-velocity impact, Icarus 31 (2) (1977) 277–288. doi:10.1016/0019-1035(77)90038-0.